UNIVERSITY OF PARDUBICE

FACULTY OF CHEMICAL TECHNOLOGY

Department of General and Inorganic Chemistry

Patrik Čermák

The influence of transition metal doping on transport and magnetic properties of Bi$_2$Se$_3$

Theses of the Doctoral Dissertation

Pardubice 2019

Study program: **Chemistry and Technology of Materials**

Study field: **Chemistry and Technology of Inorganic Materials**

Author: **Ing. Bc. Patrik Čermák**

Supervisor: **prof. Ing. Čestmír Drašar, Dr**.

Year of the defence: 2019

References

ČERMÁK, Patrik. *The influence of transition metal doping on transport and magnetic properties of Bi_2Se_3*. Pardubice, 2019. 111 pages. Dissertation thesis (Ph.D.). University of Pardubice, Faculty of Chemical Technology, Department of General and Inorganic Chemistry. Supervisor Prof. Ing. Čestmír Drašar, Dr.

Abstract

The present thesis is focused on study of the effect of transition metal doping on transport and magnetic properties of bismuth selenide. For this purpose, elements of 6th group, chromium and molybdenum, were chosen. Single-crystalline samples were prepared in two sets of composition: a) $Bi_{2-x}Cr_xSe_3$, where x=0-0.04, and b) $Bi_{2-x}Mo_xSe_3$, where x=0-0,05. Samples were characterized by the X-ray diffraction analysis (both, common and high resolution), scanning electron microscopy equipped with energy dispersive analyzation (SEM EDS), atomic force microscopy (AFM), measurement of electrical conductivity σ, Hall coefficient R_H and Seebeck coefficient α, and eventually magnetic susceptibility. Both systems show remarkable material features and interesting thermoelectric properties.

Abstrakt

Práce je věnována studiu vlivu přechodných kovů na transportní a magnetické vlastnosti selenidu bismutitého. Pro tento účel byly vybrány prvky VI. skupiny, chrom a molybden. Byly připraveny dvě kompoziční řady vzorků v monokrystalické formě: a) $Bi_{2-x}Cr_xSe_3$, kde x=0-0,04, a b) $Bi_{2-x}Mo_xSe_3$, kde x=0-0,05. Připravené vzorky byly charakterizovány rentgenovou difrakční analýzou (práškovou i s vysokým rozlišením), skenovací elektronovou mikroskopií vybavenou energiově disperzním analyzátorem (SEM EDS), rentgenovou fluorescencí (XRF), mikroskopií atomárních sil (AFM), měřením měrné elektrické vodivosti σ, Hallova koeficientu R_H a Seebeckova koeficentu α, popř. i magnetické susceptibility χ. Oba systémy vykazují pozoruhodné materiálové vlastnosti se zajímavými vlastnostmi termoelektrickými.

Keywords

Bismuth selenide, Bi_2Se_3, transition metals, single crystals, doping, defects, transport properties, magnetic properties, thermoelectrics.

Klíčová slova

Selenid bismutitý, Bi_2Se_3, přechodné kovy, monokrystaly, dopování, defekty, transportní vlastnosti, magnetické vlastnosti, termoelektřina.

Table of Contents

Introduction

Bismuth selenide (Bi_2Se_3) is a layered semiconducting compound of $M_2^VX_3^{VI}$ family (where M = Bi, Sb a X = Te, Se a S). These compounds have been deeply studied for many years because of several important issues. First, Bi_2Se_3 is representative material of the family of traditional thermoelectric (TE) materials that have been used for a long time in the thermoelectric power generation and thermoelectric refrigeration applications. Bi_2Se_3 is one of the components of the Bi_2Te_3-Bi_2Se_3 solid solutions used as *n*-type branches of the thermoelectric modules operating in the temperature range of up to 300 K. However, these solid solutions are essentially based on Tellurium which is costly owing to its low abundance. Therefore, replacement of Te by the more abundant Se (or S) to obtain a cost-effective alternative material is desirable.

Bi_2Se_3 (Bi_2Te_3) adopts a rhombohedral layered crystal structure belonging to the $R\bar{3}m$ space group. The structure is formed by a periodic arrangement of the layers stacked perpendicular to the *c*-axis. Each layer is composed of five atomic planes – quintuple layers (QL) arranged in the sequence …Se^1-Bi-Se^2-Bi-Se^1…, where (1) and (2) refer to different lattice positions. The bonding between the Se^1 atomic planes is of a weak van der Waals (vdW) nature with a slight admixture of covalent bonding. Although both compounds are normally n-type semiconductors, Bi_2Te_3 can be easily tuned to be either of *n*- or *p*-type via fine-tuning of the nonstoichiometric Bi/Te ratio. On the other hand, in the as-grown Bi_2Se_3, the strong dominance of Se vacancies V_{Se} gives rise to an unintentional *n*-type bulk doping which hinders *p*-type doping.

It has been proved that some of these "tetradymite" materials are so called Diluted Magnetic Semiconductors (DMS) if they are doped with specific transition metals (TM). However, interaction leading to magnetic ordering is still subject of discussion [1–6]. The reason is the presence of two or more interactions in each sample doped with transition metal. The discovery that these materials are 3D Topological Insulators (TI) [7–11] lead to renewed attention in field of doping of these materials by elements (transition metals), which could lead to magnetic ordering.

Among many other materials is Bi_2Se_3 promising material for electronic applications as its surface states consists of a single Dirac cone in its Brillouin zone and this material has relatively wide band gap which could eventually guarantee very low bulk electric conductivity. Lowering the Fermi level toward the intrinsic regime is an important goal for exploration of its topological properties [e.g. 12]. One of the most common ways to control the Fermi level and manipulate charge carriers is by using chemical doping with a suitable external acceptor that is able to compensate the electrons.

Doping of Bi_2Se_3 by transition metals seems to be important in terms of transport and possible magnetic and topogical properties. For this purpose, we decided to explore the systems, where both dopants belong to the 6th group of transition metals:

(1) $Bi_{2-x}Cr_xSe_3$, where *x* = 0, 0.005, 0.01, 0.02, 0.03 a 0.04

(2) $Bi_{2-x}Mo_xSe_3$, where *x* = 0, 0.0025, 0.005, 0.0075, 0.01, 0.02, 0.03 a 0.05

Materials in single crystalline form were prepared. Samples were characterized by X-ray diffraction (powder and with high resolution), Scanning Electron Microscopy equipped with Energy Dispersive X-ray Spectroscopy (SEM EDS), X-ray fluorescence

(XRF), atomic force microscopy (AFM), measurement of electrical conductivity σ ($i \perp c$), Hall coeficient R_H ($B \| c$) and Seebeck coefficient α ($\Delta T \perp c$), and eventually magnetic susceptibility χ ($B \| c$ and $B \perp c$).

1   Doping, motivation and objectives

With regards to extrinsic doping, known donors in case of Bi_2Se_3 are heavier halogens, Ge, Pb and Cu [13]. Cd [14] a Hg [15] are on the contrary acceptors. Presently were discovered many acceptor impurities which lead to *p*-type electrical conductivity, e.g. co-doping of Pb and Sb on the Bi sites [16] or by atoms Ca [17], Cd [18], Mn [19, 20], Mg [21, 22] and Pb [23] or co-doping with Fe a Ca [24]. Lowering of the free electron concentration was observed upon doping with Ni [25] and Co [26]. Nevertheless there is suspicion that natural defects Bi_2Se_3 exist in the presence of these chemical acceptors. Thus, we do not know if the *p*-type material is compensated or if acceptor impurities are only "lowering" donor behavior of natural defects.

Common feature of these works dedicated to doping by transition metals is above all manipulation with spin. Ferromagnetism (FM) in chromium doped $Bi_{2-x}Cr_xSe_3$ ($0.01 \leq x \leq 0.3$) [27, 28] or chromium intercalated (maximum $T_C = 20\,K$ at 5.2% Cr) [29] Bi_2Se_3 was described in case of thin films prepared by Molecular Beam Epitaxy (MBE). On the contrary antiferromagnetic (AFM) behavior was found in case of one single crystalline sample of chromium doped Bi_2Se_3 ($Bi_{1,85}Cr_{0,15}Se_3$) [30]. Theoretical calculations [31] predict both AFM and FM ordering depending on Cr concentration in Bi_2Se_3 which can be limited by element solubility.

All papers differ in properties and solubility of magnetic impurity whereas authors admit that interaction leading to magnetic ordering is still unclear and calls for further studies. Alongside there are profound theoretical calculations regarding formation energy of intrinsic defects as V_{Se}, Bi_{Se} a Se_{Bi} [e.g. 32] which are very helpful as a guide in description of tendencies of formation of extrinsic defects alongside periodic table (e.g. V, Cr, Mn and Fe).

Although Ref. [32] suggests a slightly negative formation energy of Cr point defects in place of Bi, Cr_{Bi}, (i.e., spontaneous formation of such defects), we found the actual concentration of Cr is always lower than the nominal one in our single crystals, which indicates the opposite. Moreover, we found a tendency of clustering when the single crystals are forced to incorporate higher concentrations of Cr during growth from a Cr-rich melt e.g., in Bridgman crystal. In addition, other phases ($BiCrSe_3$, $Bi_2Cr_4Se_9$) appear for $x \geq 0.02$ in the XRD patterns of our single crystals. This is in accordance with the phase diagram indicating the solubility of Cr in the solid Bi_2Se_3 is close to zero, while the liquid state Bi_2Se_3 dissolves up to 20 % of Cr_2Se_3 at 1170 K [33]. Two incongruent compounds are formed in the pseudo-binary phase diagram: the daltonide $Bi_2Cr_4Se_9$, and the berthollide with an approximate composition of $BiCrSe_3$ (γ-phase, $Bi_5Cr_4Se_{13}$). An extraordinary paramagnetism (PM) is reported in Bi-Cr-Se ternary misfit-layer compounds based on these two compounds [34].

Following these results, we firstly aim to prepare single crystals $Bi_{2-x}Cr_xSe_3$ as close to equilibrium as possible for a given temperature to provide a detailed comparison for theoretical and experimental works. The motivation is to provide more

insight into the TM-doped "tetradymites". There are many uncertainties, including that the equilibrium solubility is lower than that expected from the theoretical predictions. Contrary to some papers [27–30], our results suggest that both AFM and FM ordering exist next to PM in this material. Notably, we show that doping with TM might be interesting in terms of TE applications. Namely, TMs are candidates for extra energy filtering of free carriers, which is a way to increase the efficiency of TE materials [35–37]. We think that nano-structuring may explain the extraordinary behavior of transport properties (Seebeck coefficient and mobility of free charge carriers).

We were aware that many questions were not satisfyingly answered and we decided to continue the study of behavior of elements of 6th group. In case of Mo doped Bi_2Se_3 we can predict, based on theoretical calculations [38], lowering band gap towards metallic state (Bi_2Se_3-10% Mo). Mentioned paper predicts strong AFM ordering with relatively high magnetic moment (2.96 µB) which could be used in field of topological superconductors. In case of $Bi_{2-x}Mo_xSe_3$ (and $Bi_{2-x}Cr_xSe_3$) we observed a pronounced increase in the mobility, which contradicts the very doping process. Further, we observed a large power factor $PF=\sigma\alpha^2 \geq 2$ $mWm^{-1}K^{-2}$ over a wide temperature range of 150-400 K. The doping effect is more pronounced for Mo doped Bi_2Se_3 than for Cr-doped Bi_2Se_3.

Our work thus provides some insights into chemistry and physics against on the background of the native defects that play a remarkable role in Bi_2Se_3 [39]. To our best knowledge, such a study is absent in literature.

2   Experiment

Single crystals of $Bi_{2-x}Cr_xSe_3$ and $Bi_{2-x}Mo_xSe_3$ with nominal x values between 0 and 0.05, were grown by heating stoichiometric mixtures of 5N Bi, Se and Cr_2Se_3 and $MoSe_2$. The synthesis of Cr_2Se_3 was carried out by heating stoichiometric mixtures of 5N purity elements at 1300 K for 7 days in quartz ampoules (all from Sigma-Aldrich). The crystal growth process involved cooling from 1043 K to 823 K at a rate of 6 K per hour. The crystals were then annealed for 350 hours at 823 K in the same ampoule and then quenched in air. This free melt crystallization (FMC) produces single crystals that are 10–20 mm in length, 3–6 mm wide and up to 3 mm thick. In addition, $Bi_{2-x}Cr_xSe_3$ single crystals were grown using the Bridgman technique (BT) to better understand the behavior of Cr during the growth. Contrary to FMC, the BT shows a directional crystallization par excellence. Thus, the liquidus–solidus distribution coefficient of the dopant in the Bi_2Se_3 plays an important role. Mostly, the solubility of the doping TM is higher in the liquid phase, as is in case of Cr, and the liquid phase becomes richer in Cr along the direction of crystal growth. Thus, the concentration of chromium increases along the single crystals up to the highest solubility, after which precipitates are eventually formed at a given temperature. The BT produces single crystals up to 60 mm in length, 8 mm wide and 5 mm thick.

For the physical property measurements, the FMC specimens with dimensions of 10–15 × 3 × (0.1–0.2) mm^3 were cut from the single crystals. The actual doping level and macroscopic homogeneity were examined using XRF mapping with a µ-XRF spectrometer M4 TORNADO (Bruker), Rh-50 keV, equipped with polycapillary X-ray optics. To reveal the microscopic homogeneity, we employed energy dispersive X-ray

microanalysis (EDS) using scanning elektron microscopy (SEM) LYRA 3 (Tescan) equipped with an EDS analyzer Aztec X-Max 20 (Oxford Instruments). The diffraction patterns (Cu Kα, λ = 1.5418 Å) were recorded on powdered samples using a D8 Advance diffractometer (Bruker AXES, Germany) with a Bragg–Brentano Θ-Θ goniometer (radius 217.5 mm) equipped with a Ni-beta filter and a LynxEye detector. The scans were performed at room temperature from 10 to 90° (2Θ) in 0.01° steps with a counting time of 2 s per step. The lattice parameters were refined using the Le Bail method as implemented in the program FullProf.

High-resolution X-ray diffraction (HRXRD) on single-crystalline $Bi_{2-x}Cr_xSe_3$ samples was carried out on a PaNalytical Expert-Pro diffractometer, equipped with a sealed CuK_α tube, primary parabolic multilayer optics, a 2x220Ge single-crystal monochromator, a 3x220Ge analyzer, and a proportional point detector. Using this high-resolution setup, we were able to measure the reciprocal-space distribution of the diffracted intensity with a resolution down to 10^{-4} Å^{-1}.

The topology and phase shift images of the freshly cleavaged surface of the highest layer were measured by the AFM SolverPro M (Nt-MDT, Russia) with a resolution of 512x512 pixels. The HA_NC tips (resonant frequency 140 kHz, force constant 3.5 N/m) were used for the measurements.

The transport parameters include the electrical conductivity $\sigma(i\perp c)$, the Hall coefficient $R_H(B\|c)$, and the Seebeck coefficient $\alpha(\Delta T\perp c)$. These parameters were measured in the direction perpendicular to the trigonal axis, c, i.e., the electric field and thermal gradients were applied in the basal plane while the magnetic induction vector was parallel to the c axis. All parameters were measured over a temperature range from 80 K to 470 K, and a conductive graphite adhesive was used to attach the current leads. Platinum wires (50 μm in diameter) were attached along the sample using thermocompression to measure the voltage drop. The Hall effect and electrical conductivity were examined using a lock-in nano-voltmeter with a 29-Hz excitation and a static magnetic field of 0.6 T. The Seebeck coefficient was determined using the longitudinal steady-state technique with a temperature difference ranging from 3 to 3.5 K. The thermal gradients were measured with the aid of fine copper-constantan thermocouples. The magnetic properties were investigated using an MPMS apparatus (Quantum Design).

3 Bi₂Se₃ doped with Cr

$Bi_{2-x}Cr_xSe_3$ had been studied in composition range $x = 0$, 0.005, 0.01, 0.02, 0.03, and 0.04 (nominal).

3.1 Powder X-ray diffraction (PXRD)

Typical X-ray diffraction patterns of $Bi_{2-x}Cr_xSe_3$ obtained for powdered single crystals are shown in Fig. 2. Although all the diffraction peaks can be attributed to the structure of the Bi_2Se_3 for $x \leq 0.01$, there is clear evidence of additional phases (one peak at 2Θ

= 31.3° attributable to both the $Bi_2Cr_4Se_9$ and γ-phase (approximate composition $BiCrSe_3$)) at x = 0.03 and x = 0.04. This peak is barely detectable for a nominal composition $Bi_{1.98}Cr_{0.02}Se_3$, even for very fine measurements. Thus, the equilibrium solubility of Cr in Bi_2Se_3 at 820 K lies below x = 0.02. For the TE, this is the nominal concentration over which the micro-precipitates (X-ray detectable) of other phases might form. Thus, the nano-precipitates might form at far lower Cr concentrations depending on the growth kinetics. The lattice parameters of the parent material, a = 0.41387 nm and c = 2.86303 nm, are in good agreement with those in the database (PDF-4+/ICDD). We observe that the lattice parameters decrease moderately with the increase of the Cr concentration.
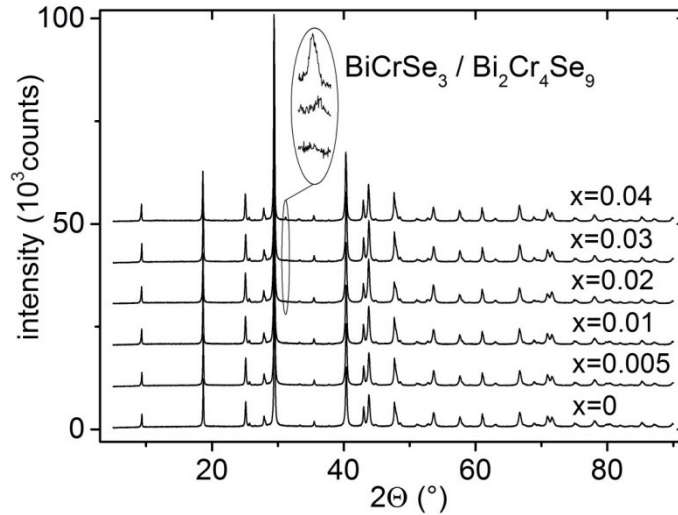

Fig. 1. XRD patterns of $Bi_{2-x}Cr_xSe_3$ single crystals for nominal x = 0–0.04. There is clear evidence of an additional phase (peak at 2Θ = 31.3°) for x = 0.03 and 0.04, which can be attributed to either $BiCrSe_3$ or $Bi_2Cr_4Se_9$. This peak is barely detectable for nominal x = 0.02. The patterns are shifted vertically for clarity.

3.2   High resolution X-ray diffraction (HRXRD)

To visualize randomly rotated mosaic blocks, we measured the reciprocal-space maps around the main maximum 000.15 of the $Bi_{1.99}Cr_{0.01}Se_3$ sample and of a pure Bi_2Se_3 single crystal (Fig. 2). Fig. 3(a,b) shows the linear scans extracted from the measured maps along the Q_x and Q_z axes, respectively. The reciprocal-space maps demonstrate the good crystal quality. The horizontal diffuse elongation of the diffraction maxima can be observed in both the $Bi_{1.99}Cr_{0.01}Se_3$ and Bi_2Se_3 samples, which is caused by randomly rotated mosaic blocks. Nevertheless, in both investigated samples, the main maximum is approximately 100 times higher than the diffuse peak. From this fact, we conclude that the majority of the sample volume is not rotated, and the rotated blocks make up less than approximately 1% of the total irradiated volume. Detailed inspection of the data reveals two interesting features that are visible mainly in the Q_x-scans from Fig. 3(a). The curve of sample $Bi_{1.99}Cr_{0.01}Se_3$ always contains a rather sharp side maximum (blue arrow in Fig. 3(a)). This maximum most likely stems from

a misoriented large mosaic block. The degree of the block misorientation can be estimated as 0.26° with respect to the surrounding crystal matrix, and its lateral size can be compared to the coherence width of the primary X-ray beam, i.e., 0.5–1.0 μm. A similar feature can be found on the Q_x-scan of Bi_2Se_3 [red arrow in Fig. 3(b)]. The interpretation of this effect is complicated and might be caused by many misoriented blocks (misorientation on the order of 1°). Thus, the blocks are probably very small in the lateral direction (tens of nm). Fig. 3(b) shows the vertical (Q_z-) scans extracted from Fig. 2. The Q_z-scans of both samples are very similar, and their widths are comparable to the experimental resolution. This finding indicates that the distances of the (0001) basal planes in the rotated mosaic blocks and in the main crystal are the same, i.e., the local lattices of the blocks are only rotated and not strained. The physical nature of these blocks is not clear. For example, they can be created by laterally small faults in the stacking of the Bi-Se basal atomic planes (stacking faults or twins). The effect of the dislocations is less likely, since no deformation of the block lattices was observed.
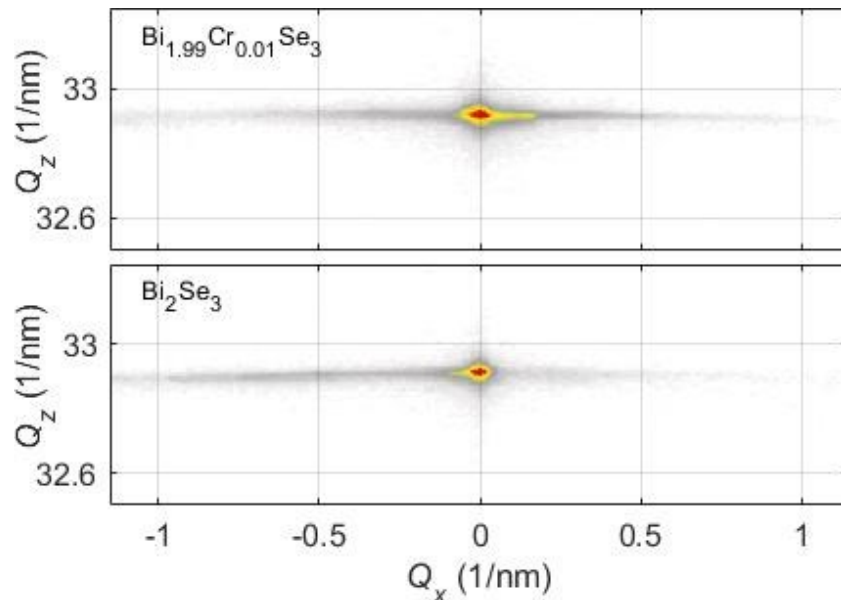

Fig. 2. High-resolution XRD reciprocal-space maps measured around the 000.15 reciprocal-lattice points of the single crystals $Bi_{1.99}Cr_{0.01}Se_3$ (top panel) and Bi_2Se_3 (bottom). The color scale covers four decades of scattered intensity.
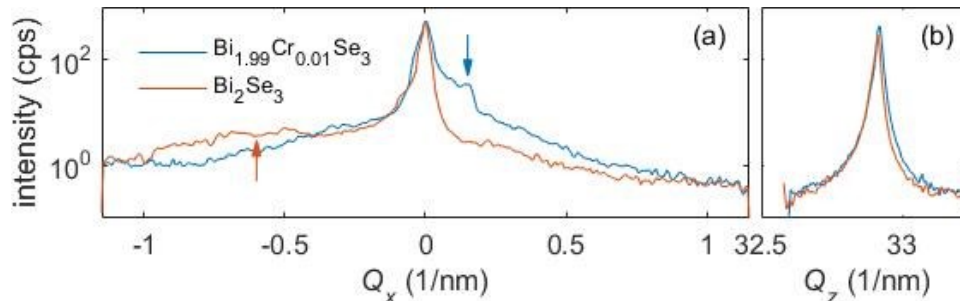

Fig. 3. The linear scans extracted from the reciprocal-space maps in Fig. 4 along the horizontal (a) and vertical directions (b). The arrows denote the features discussed in the text.

3.3   XRF analysis

Fig. 4 shows the XRF mapping ($\approx$ 100 μm mean penetration depth) of the cleaving plane of the BT single crystals. In fact, we observed random cluster formation in all studied single crystals for $x \geq 0.01$, although the occurrence decreases markedly with the drop of the Cr content. Furthermore, the increasing concentration of Cr is apparent towards the end of the BT crystal, which indicates a higher solubility of Cr in liquid rather than in the solid phase. In fact, the actual solubility of Cr in the Bi_2Se_3 samples is lower according to the XRF analysis, as summarized in Table 1. Thus, we cannot conclude on the true solubility of Cr based on this analysis. Magnetic measurements suggest the maximum solubility is $x_{MAX} \leq 0.003$ (for samples annealed at 823 K), as described below. Thus, we expect a formation of nano-precipitates, which are not detectable by powder XRD, for $x \geq 0.003$. From this perspective, the composition and properties of a sample will strongly depend on its thermal history. We use single-crystalline samples prepared from the inside of a batch since the surface might contain Cr-rich phases.
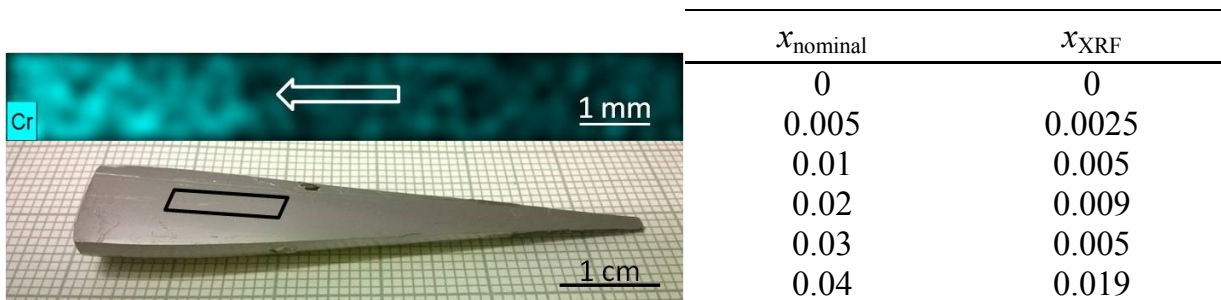

$x_{nominal}$	x_{XRF}
0	0
0.005	0.0025
0.01	0.005
0.02	0.009
0.03	0.005
0.04	0.019

Fig. 4. XRF mapping of chromium (top) in the $Bi_2Cr_{0.01}Se_3$ BT grown single crystal (bottom; black rectangle corresponds to the analyzed area). The strong inhomogeneity in the Cr distribution is evident. Note that the Cr concentration increases towards the Bridgman crystal end (head), which indicates that the solubility of Cr is higher in the liquid phase than in the solid phase. Table1. Comparison of nominal concentration of Cr with concentration obtained from XRF in $Bi_{2-x}Cr_xSe_3$ FCM grown single crystals.

3.4   SEM/EDS analysis

We use the SEM/EDS analysis as a complementary method to XRF with a much lower penetration depth, which limits the information depth. Contrary to XRF, the EDS analysis of the samples shows a lower if not zero concentration of Cr on the surface of a single crystal, independent of its composition. We performed many scans to discover areas showing higher than zero concentrations, since such areas are randomly embedded throughout the crystal volume. We succeeded at the head of the BT crystal, where such precipitates form frequently due to growth from the Cr-rich melt and occur more frequently just beneath the surface. Such a scan is depicted in Fig. 5. Expectedly, the concentration from the EDS analysis depends on the accelerating voltage U of the electron beam. While we obtain 5 at% Cr for U = 20 kV (penetration depth of electrons $\approx$ 900 nm; 80% of the EDX signal is from $\approx$ 480 nm), the U = 5 kV

(penetration depth of electrons $\approx$ 100 nm; 80% of the EDX signal is from $\approx$ 55 nm) gives 16 at% of Cr. The simulation of the penetration depth was performed with the CASINO Monte Carlo program (v2.42) [40]. This clearly indicates that the chromium forms layered inclusions within the Bi_2Se_3 matrix. Apparently, the perfect layered structure of the Bi_2Se_3 matrix is not affected by the presence of Cr (Fig. 5).
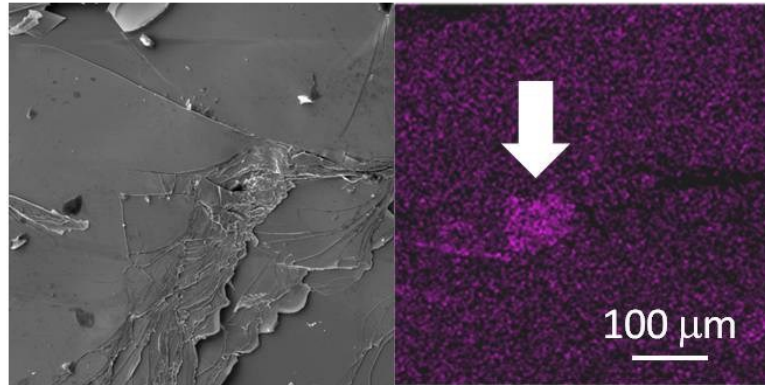

Fig. 5. The SEM/EDS mapping of chromium in $Bi_{2-x}Cr_xSe_3$ BT-grown single crystals.

3.5   Atomic force microscopy (AFM)

AFM measurements provide high-resolution scanning of the crystal surface. The AFM mappings were always performed on a fresh surface after peeling off/cleavage of a thin layer with an adhesive tape. Cr tends to form homogeneously dissipated nanoscale defects (precipitates/nanoinclusions) with a height of a couple of nm and lateral dimensions of tens to hundreds nm (Fig. 6). In contrast to the Mo doped sample, the Cr-precipitates appear after each 5 to 10 peelings. This suggests that either the Cr-based precipitates increase the adhesion of adjacent Bi_2Se_3 layers or that they are distributed less homogeneously.
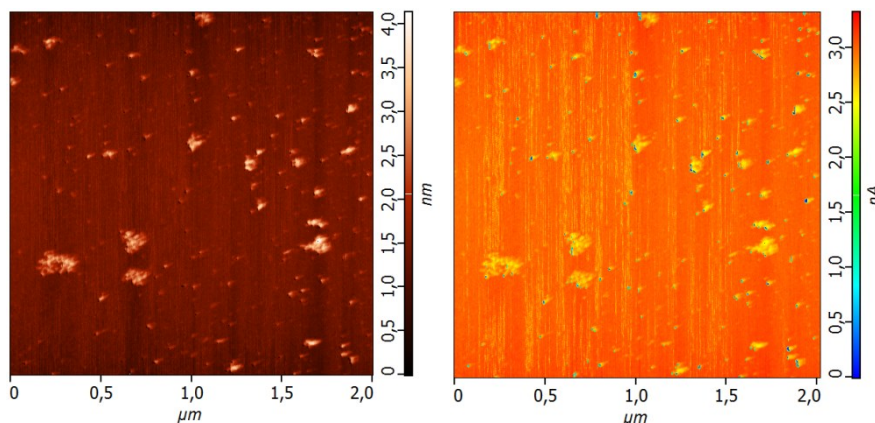

Fig. 6. Found defects/precipitates after several peeling off/cleavage of a thin layer of the sample analyzed by AFM. Brown scale means topography, blue-red scale means phase image. We have found defects/precipitates with a height of a couple of nm and lateral dimensions of tens to hundreds of nm. Analysis was performed on single crystal $Bi_{1,98}Cr_{0,02}Se_3$.

3.6　Transport properties

For sake of brevity we do not present all measured data here. Fig. 7 presents the logarithmic temperature dependence of Hall mobility. Exponent r becomes close to −1.5 (solid line in Fig. 7) irrespective of the doping, which indicates scattering by acoustic phonons. All parameters provide evidence for the acceptor characteristics of chromium, although the actual doping efficiency remains fairly low ($\approx 10\%$). This indicates the formation of both Cr_{Bi}^{-1} (chromium effectively in the Cr^{+2} state) and Cr_{Bi} (chromium effectively in the Cr^{+3} state). This is in accordance with the measurement of the magnetic susceptibility, which reveals the formation of the high spin of Cr^{+2}. Contra-intuitively, the mobility of the Cr-doped samples ($x \leq 0.01$) is higher than the mobility of pure Bi_2Se_3. This suggests some healing process leading to the increasing scattering times. We conclude that Cr reduces the amount of the two dominant defects: Se vacancies V_{Se} and Bi anti-sites in the place of Se, Bi_{Se}. In fact, the healing process could account for the acceptor-like effect in terms of the shift in the host native defect equilibrium:

$$Bi_{Bi} + V_{Se}^{+2} + 2e^- \Leftrightarrow Bi_{Se}^{-1} + V_{Bi}^{-3} + 4h^+ \tag{1}$$
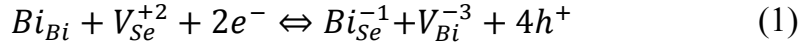
However, in view of the magnetic measurements, we also attribute the doping effect to the formation of the Cr^{+2} state. Next to substitution, Cr^{+2} can be a part of Cr-rich nano-/micro-inclusions within the vdW gap.
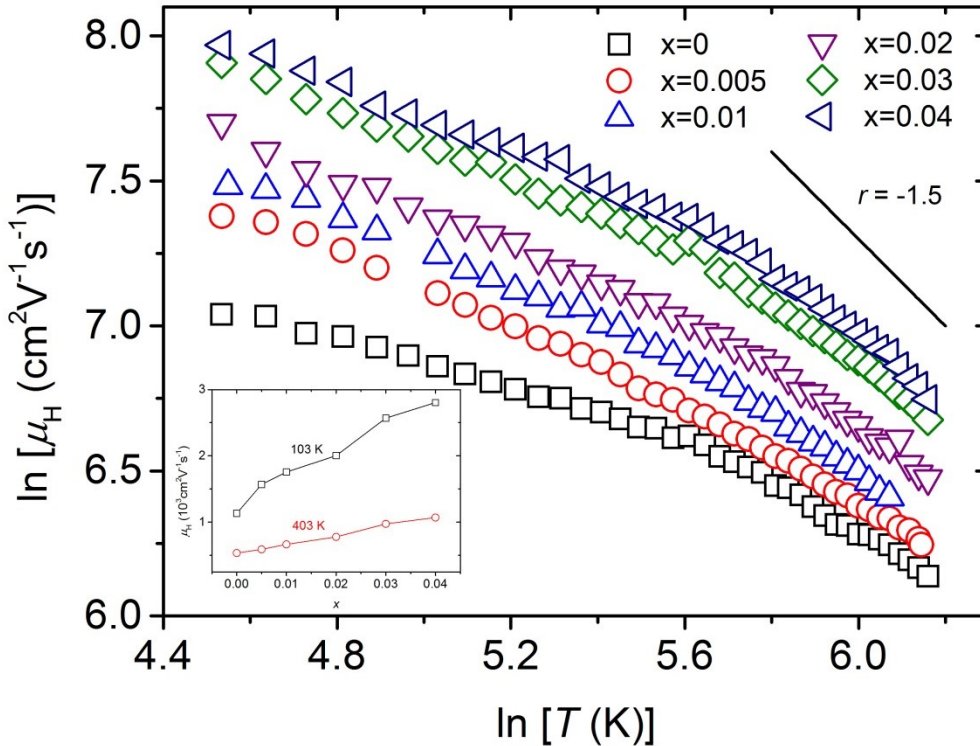

Fig. 7. Hall mobility as a function of temperature in a natural log-scale for the $Bi_{2-x}Cr_xSe_3$ single crystals. The solid line corresponds to scattering of acoustic phonons. Note that the scattering of acoustic phonons dominates above T = 400 K, irrespective of the doping. Inset: Hall mobility as a function of the concentration x for the $Bi_{2-x}Cr_xSe_3$ single crystals for two different temperatures.
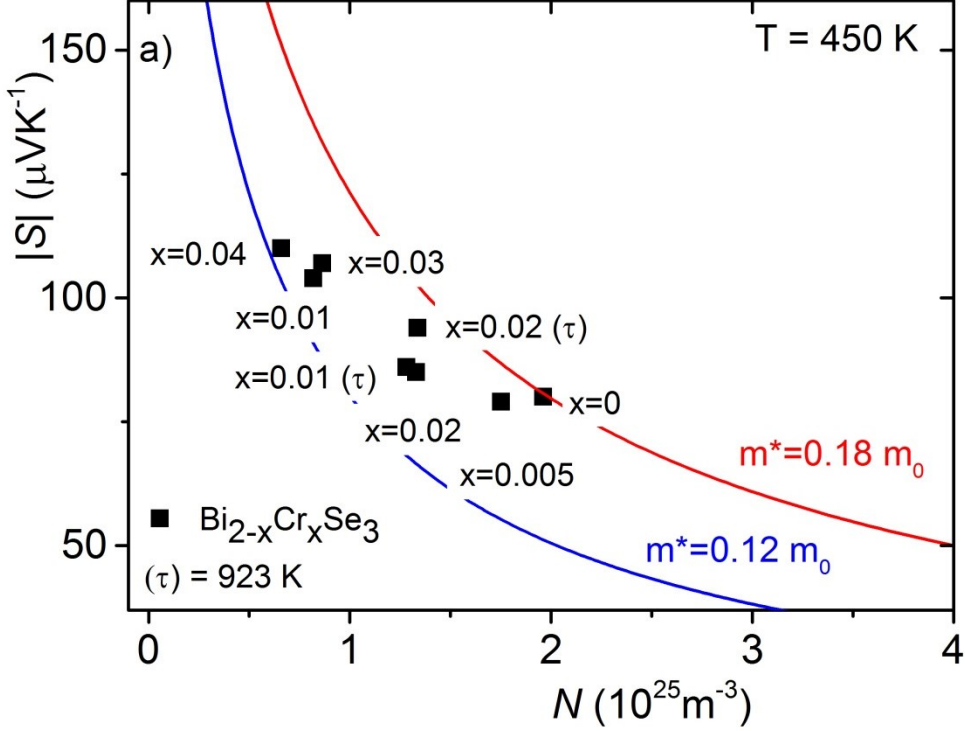
13

Fig. 8. Seebeck coefficient as a function of the Hall carrier concentration for $r_H = 1$ (Pisarenko plot) for the $Bi_{2-x}Cr_xSe_3$ single crystals at T = 450 K. The τ denotes samples annealed at 920 K.

We observe an extraordinary behavior in Cr-doped Bi_2Se_3. Fig. 8 shows the Seebeck coefficient as a function of the FC concentration (*Pisarenko plot*). These curves all indicate an extraordinary behavior showing that the Seebeck coefficient does not follow the theoretical curve. The experimental slope of the function $\alpha = f(n)$ is higher than the theoretically predicted value, which prevents the explanation in terms of the increasing effective mass.

We believe these results could indicate the extraordinary energy filtering of free electrons. We suggest three possible mechanisms:

1. Energy selective capture of an electron due to the mixed valence state Cr^{+2}/Cr^{+3} or the formation of the Cr-based nano-precipitates which can lead to the energy-dependent scattering of electrons.
2. The effect of the mosaicity feature, i.e., the formation of nano-structures due to small variations in the tilt of the trigonal axis c along single crystals in the Cr-doped crystal.
3. Decrease/formation of Se vacancies and Bi anti-sites which are effective ionized scattering centers.

Importantly, the extraordinary behavior could be observed for samples $x = 0.01$, 0.02 and 0.03. For these three samples, the maximum of the Seebeck coefficient α and the PF tends to be higher compared to pure Bi_2Se_3, although apparently shifted towards higher temperatures (Fig. 9). Namely, such a shift of the α-maximum towards

14

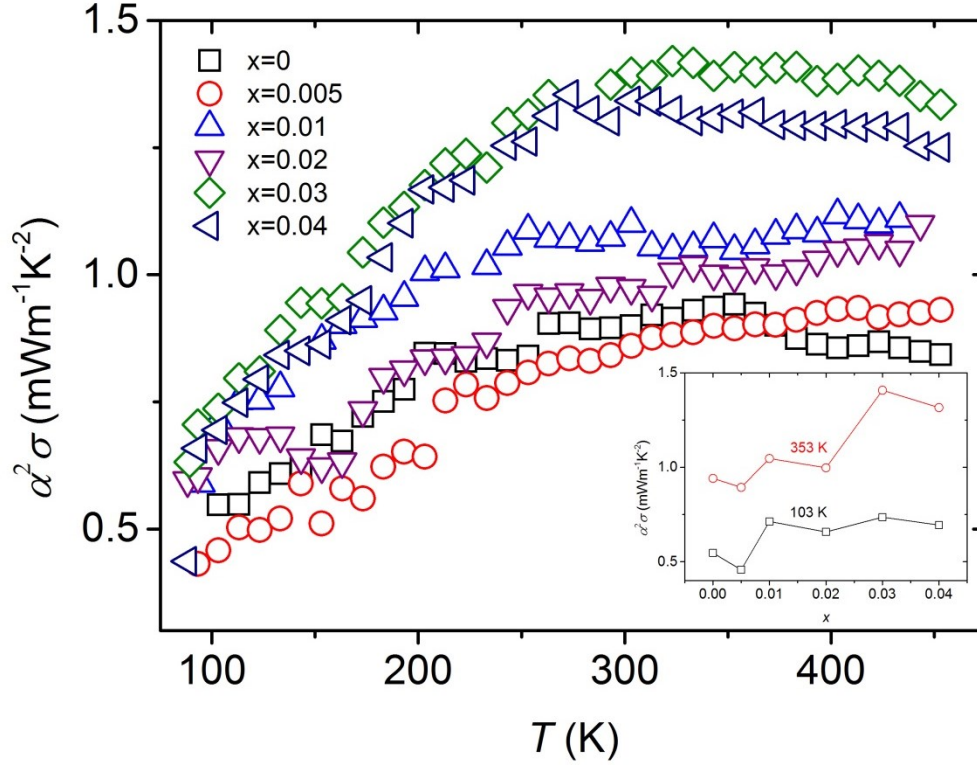higher temperatures is linked to an increase of the FC concentration and decrease of α in ordinary systems.

Fig. 9. Power factor as a function of temperature for the $Bi_{2-x}Cr_xSe_3$ single crystals. Inset: Power factor as a function of the concentration x for the $Bi_{2-x}Cr_xSe_3$ single crystals for two different temperatures.

3.7 Magnetic properties

The $Bi_{2-x}Cr_xSe_3$ samples with nominal $x = 0.005$ and actual $x = 0.0025$ show almost pure PM, indicating that chromium is truly dissolved in the matrix (Fig. 10). Even the magnetization curves show no trace of magnetic ordering. Instead, the magnetization saturates at high fields and perfectly matches the Brillouin function (Fig. 10 inset). We observe mostly the same picture for nominal $x = 0.01$ and 0.02 (actual $x = 0.005$ and 0.009). Curie-Weiss fit indicates the formation of both Cr_{Bi}^{-1} (chromium effectively in the Cr^{+2} state, $J = 2$) next to Cr_{Bi} (chromium effectively in the Cr^{+3} state, $J = 1.5$). This is in accordance with the Hall effect measurements, which reveal slight donor activity as discussed above. Curie-Weiss law is given:

$$\chi = \frac{C}{T - T_{CW}} + \chi_0 \qquad (2)$$

where

$$C = n(Cr)g_J\mu_0\mu_B^2 J_{CW}(J_{CW} + 1) \qquad (3)$$

where χ is the magnetic susceptibility, C is the Curie constant, T_{CW} is the critical paramagnetic temperature and χ_0 is a temperature independent term that considers the mostly diamagnetic contributions of the host lattice, Landé factor is $g_J = 2$ for orbital

15

quenching, and μ_0 and μ_B are the vacuum susceptibility and Bohr magneton, respectively.
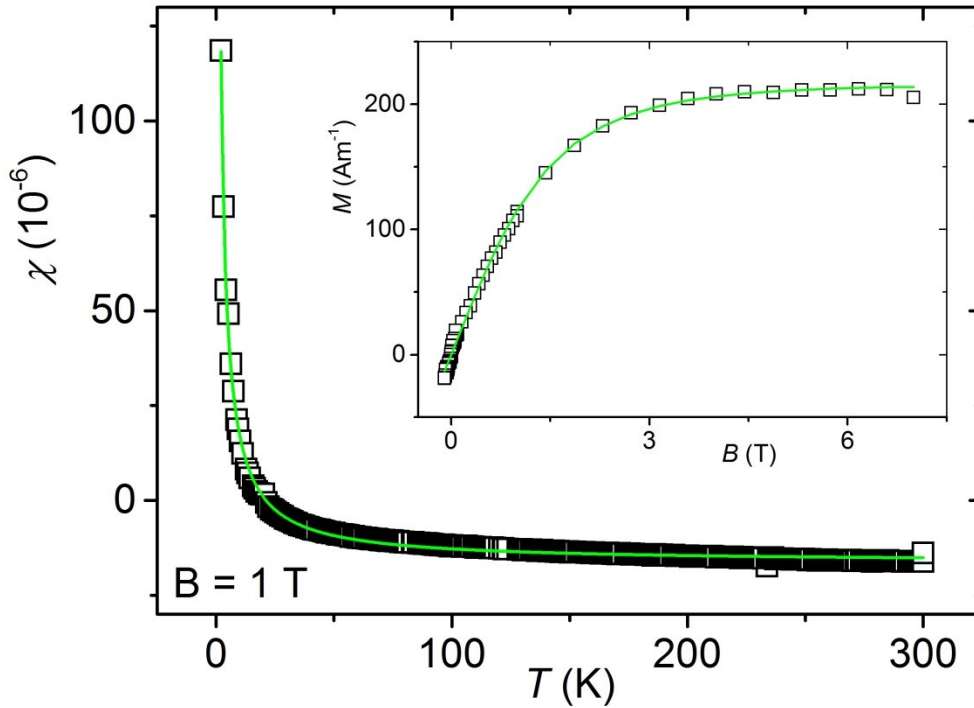

Fig. 10. Susceptibility as a function of temperature for the Bi$_{2-x}$Cr$_x$Se$_3$ single crystal with a nominal x = 0.005. The solid curve is a fit to the Curie–Weiss law. Inset: Magnetization as a function of the magnetic field strength for the Bi$_{2-x}$Cr$_x$Se$_3$ single crystal with a nominal x = 0.005. The solid curve represents the fit to the Brillouin function. The diamagnetic part proportional to field B was subtracted from the experimental values.

Rather complex magnetic properties are observed for one sample Bi$_{2-x}$Cr$_x$Se$_3$ with a nominal $x = 0.04$ (Fig. 15). While the high-temperature data CW fit gives a positive T_{CW}, i.e., an FM ordering, the CW fit of the low temperature data gives a negative T_{CW}, i.e., an AFM ordering. Thus, we have two competing interactions, FM and AFM, on the PM background of the diluted Cr solid solution – a lone substitutional Cr$_{Bi}$ defect in the Bi$_2$Se$_3$ matrix (see inset in Fig. 11). Interestingly, the χ = f(T) is almost independent of the orientation, i.e., the results differ within measurement accuracy for in-plane and cross-plane magnetic field orientations. Strikingly, we observe the effect of the magnetic field strength (Fig. 11). Such a peculiar behavior calls for a thorough study on an even larger set of samples and is beyond the scope of this thesis.
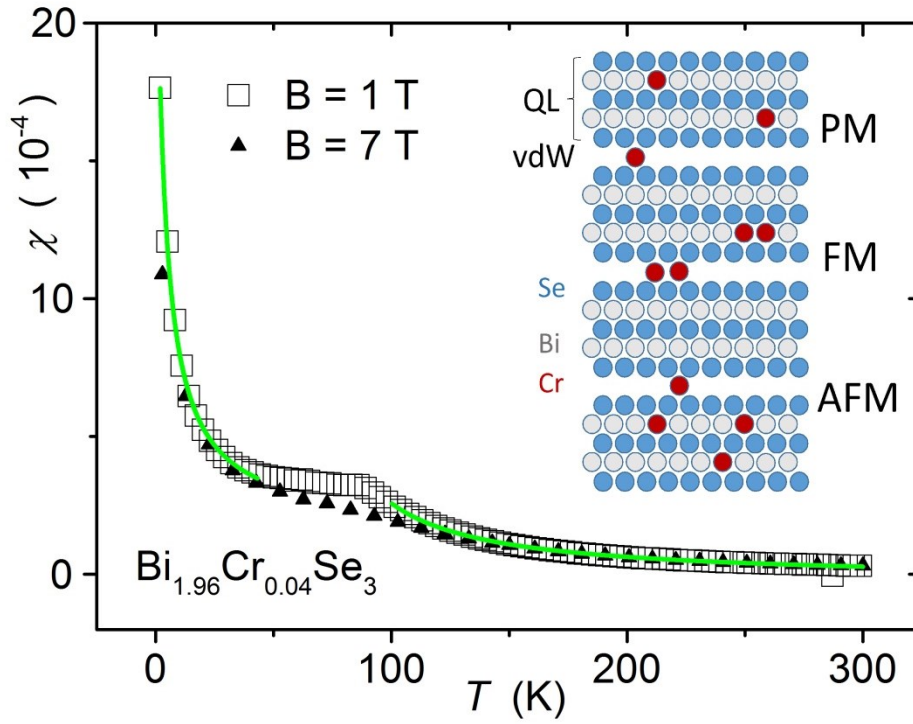
Fig. 11. Susceptibility as a function of temperature for the $Bi_{1.96}Cr_{0.04}Se_3$ single crystal for B = 1 and 7 T. The solid lines are the fits according to the CW law. Inset: Three ways of embedding a small number of Cr atoms within the quintuple layers (QL) or between QL – in the vdW gap of Bi_2Se_3 leading to PM, FM, and AFM state.

4 Bi_2Se_3 doped with Mo

$Bi_{2-x}Mo_xSe_3$ had been studied in composition range x = 0, 0.0025, 0.005, 0.0075, 0.01, 0.02, 0.03 a 0.05 (nominal).

4.1   Powder X-ray diffraction (PXRD)

Powder X-ray diffraction (PXRD) patterns of $Bi_{2-x}Mo_xSe_3$ obtained for powdered single crystals are presented in Fig. 12. All of the diffraction peaks can be attributed to the structure of Bi_2Se_3 for $x \le 0.005$. There is some evidence of an additional phase (one very small peak at $2\Theta \approx 13.7°$, (002) peak of $MoSe_2$)) for $x \ge 0.0075$. This peak is barely detectable for any nominal composition starting with $Bi_{1.9925}Mo_{0.0075}Se_3$, even for very high resolution measurements. Importantly, the peak intensity increases negligibly with the increasing nominal content of Mo (inset a, Fig. 1). We observe that the lattice parameters a and c decrease slightly with the Mo concentration up to nominal x=0.01 and so does the unit cell volume (UCV) (inset b, Fig. 1). However, the observed slight decrease in the lattice parameters and UCV upon doping is within the experimental error for $x \le 0.01$. For $x > 0.01$, we observe a stepwise increase above the lattice parameters of the hosting lattice. This increase reflects the change in the stoichiometry of the hosting structure due to the precipitation of $MoSe_2$ which strongly shifts the

17

stoichiometry of the hosting structure toward the Se-poor/Bi-rich state. From the PXRD results, we conclude that the substitutional solubility of Mo in solid Bi_2Se_3 as defined by the formula $Bi_{2-x}Mo_xSe_3$ is very low ($x \leq 0.005$) in a close to equilibrium state at 550°C but increases slightly with the temperature.

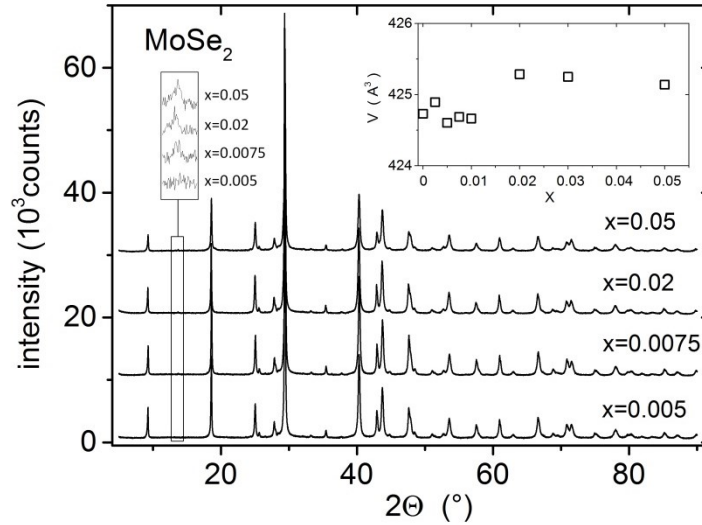*Fig. 12. XRD patterns of $Bi_{2-x}Mo_xSe_3$ single crystals. There is clear evidence of an additional phase (a peak at $2\Theta = 13.7°$) for x=0.0075 to 0.05, which can be attributed to $MoSe_2$ (inset a). This peak is undetectable for nominal Mo content x=0.005. The patterns are shifted vertically for clarity. The inset b shows the variation of the unit cell volume (UCV) with the nominal Mo content.*

4.2 High resolution X-ray diffraction (HRXRD)

Fig. 13 presents the experimental results of the doped samples. Interestingly, the horizontal streak is much more intense for the Mo concentrations of $x = 0.0025$ and $x = 0.005$ [panels (a, b)]; these samples therefore contain many more small misoriented domains than the non-doped sample (Fig. 2 bottom). In panels (c) and (d) showing the results for $x = 0.0075$ and $x = 0.02$, the intensity of the horizontal streak is comparable to that for the undoped sample, so that the relative volume of small misoriented domains is again small. In addition to these continuous horizontal streaks, panels (a-c) exhibit substantial horizontal broadening of the main diffraction maximum. This can be attributed to the presence of a few large misoriented domains (grains); it is observed that the characteristic misorientation of the domains increases with x and reaches maximum value for $x = 0.0075$. This coincides with occurrence of Bi_2 BLs (discussed below). In the sample with $x = 0.02$, such large misoriented grains are not visible. From the vertical width of the diffraction maxima it follows that the size of the misoriented grains is comparable to the coherence width of the primary X-ray beam, so that it could reach several hundreds of nm or even larger. To summarize these results, while the structural quality of the samples as seen by X-ray diffraction decreases with increasing Mo concentration x, the samples with $x \geq 0.02$ again become structurally perfect. This picture reflects the depletion/formation of point defects (Bi_i, Bi_{Se} and V_{Se}) and Bi_2 bilayers (BLs) upon Mo doping. Moreover, this conclusion is in accordance with the transport measurements; for $x \geq 0.02$, the transport properties of

$Bi_{2-x}Mo_xSe_3$ samples are comparable to those of the undoped Bi_2Se_3. The absence of the wide horizontal streaks coincides with the highest PF.
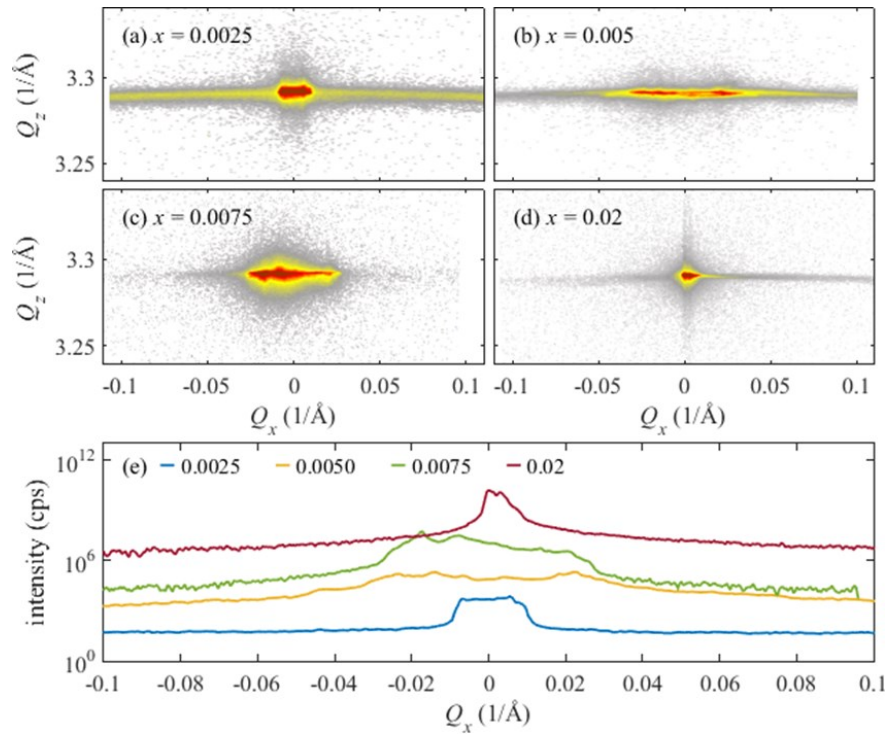

Fig. 13. Reciprocal-space maps measured around the reciprocal lattice point 000.15 of samples with various Mo concentrations x [panels (a) to (d)]. The colors span over five decades of intensity. In (e), the horizontal cuts are displayed as the maps across the diffraction maxima. The curves are shifted vertically for clarity.

4.3 SEM/EDS analysis

In Fig. 14, EDS analysis of the samples show very low (if any) concentration of Molybdenum on the freshly cleaved surface of a single crystal $Bi_{1.9925}Mo_{0.0075}Se_3$. We note that the nominal concentration of Mo lies within the detection threshold ($\approx$1 at. %) of the EDS instrument. We observe random precipitated clusters of $MoSe_2$ (according to a detailed point EDS analysis) that are embedded in the voids within the single crystal bulk or on the bulk surface (Fig. 14). The occurrence of $MoSe_2$ precipitates strongly decreases with decreasing nominal Mo concentration.
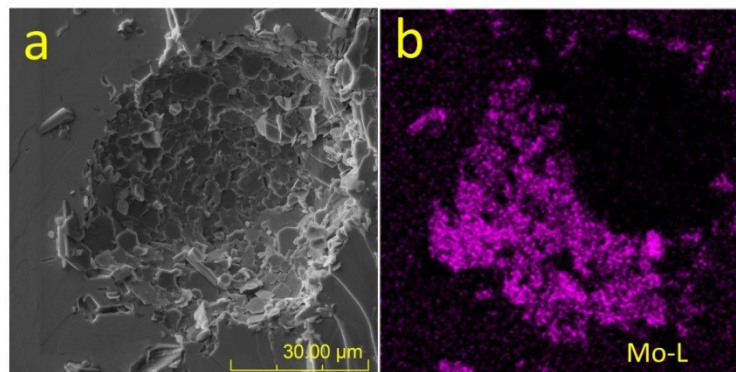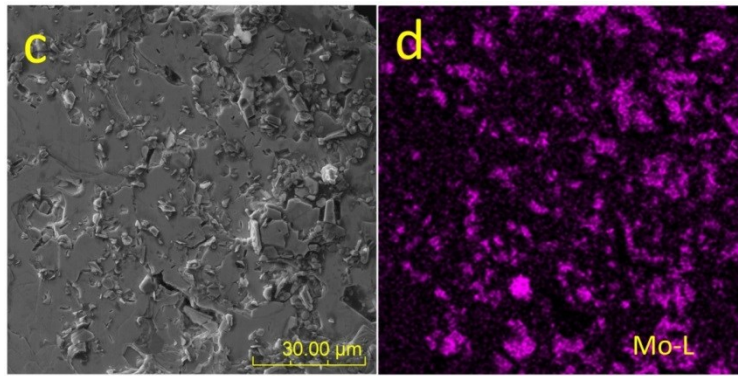
Fig. 14. a) The SEM scan of the void within a freshly cleaved single crystal with corresponding b) EDS mapping of the Molybdenum content. c) The SEM scan of the as grown surface of the single crystal and with corresponding d) EDX mapping of the Molybdenum content. All measurements were performed on $Bi_{2-x}Mo_xSe_3$ single crystals with x=0.0075. The occurrence of precipitated $MoSe_2$ within the microscopic voids makes it difficult to analyze the composition of the hosting matrix more precisely, e.g., by using atomic absorption spectroscopy.

4.4   Atomic force microscopy (AFM)

We observe layered defects ≈0.35 nm in thickness spreading laterally over relatively large areas of up to several μm. This area exhibits a contrast in a phase image, i.e., material differences in the density/adhesion or stiffness are the main reasons for the adherence of the tip on these points in contrast to the rest of the material. This strongly suggests an embedding of a bilayer (BL) of Bi_2 that has the best match to the thickness.
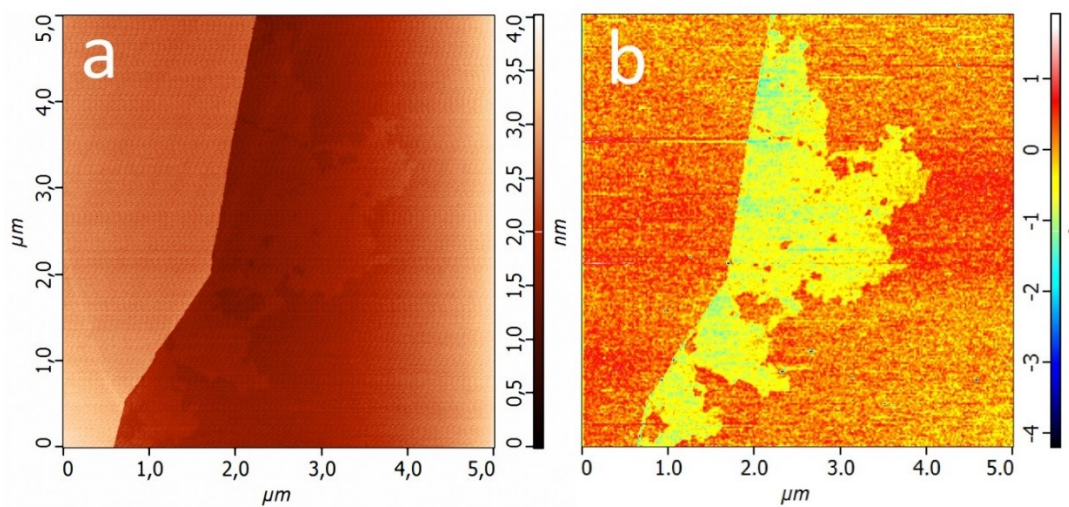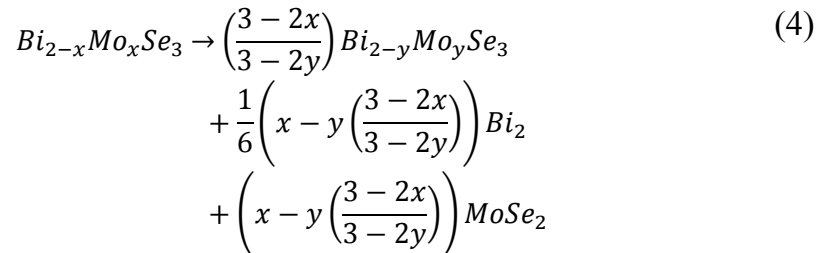

Fig. 15. a) and b) AFM topology and phase image mappings of $Bi_{2-x}Mo_xSe_3$, x = 0.0075; the height of the vertical sharp edge corresponds to Bi_2Se_3 QL (0.95 nm).

From this edge to the right, a layered defect spreads with the thickness of 0.35 nm that is comparable to the thickness of Bi_2 BL.

4.5   Transport properties

The temperature dependence of the parameters suggests an extrinsic state of all $Bi_{2-x}Mo_xSe_3$ samples. All of the parameters indicate the acceptor-like behavior of molybdenum up to $x \approx 0.01$, where all three parameters show an extremum. We obtain a low nominal doping efficiency $\eta \approx 0.2$ for $x=0.0025$ and almost constant of $\eta \approx 0.3$ for the next three samples with $x=0.005$ to 0.01 followed by almost zero efficiency for $x \geq 0.02$. Considering the very low substitutional solubility ($x \leq 0.005$), the low (and almost constant up to x=0.01) nominal doping efficiency strongly indicates an unusual interaction with the native defects. Furthermore, the mobility of the Mo doped samples ($x \leq 0.01$) increases to a value high above the mobility of the undoped Bi_2Se_3 (Fig. 16), which is counterintuitive and formally contradicts any formation of point defects. Rather, it suggests the presence of some healing process leading to the increase of the mean free paths / scattering times of free carriers (FC). The increase in the mobility results in a large power factor $PF = \sigma \alpha^2 \geq 2$ $mWm^{-1}K^{-2}$ spreading over a wide temperature range of 150-400 K (Fig. 17). To the best of our knowledge, such a high PF over such a wide temperature range has not been reported for Bi_2Se_3 to date.

Based on doping efficiency, one can estimate the substitutional solubility of $y \approx 0.001$ (see eq. (4) below). The surplus molybdenum precipitates in form of $MoSe_2$, shifting the stoichiometry toward the Bi rich/Se-poor state. The lack of Se leads to the formation of Bi_2 BLs instead of Bi interstitials, Bi_i, Bi antisites, Bi_{Se} or V_{Se} that are formed in the undoped Bi_2Se_3. The BLs, in turn, increase the binding energies within the QLs and the ionicity of the outer Se atoms in the QLs of Bi_2Se_3, essentially resulting in the reduction of native defect concentration in a "chicken and egg" scenario. The overall stoichiometry can be expressed by the following reaction:

$$Bi_{2-x}Mo_xSe_3 \rightarrow \left(\frac{3-2x}{3-2y}\right)Bi_{2-y}Mo_ySe_3 \qquad (4)$$
$$+ \frac{1}{6}\left(x - y\left(\frac{3-2x}{3-2y}\right)\right)Bi_2$$
$$+ \left(x - y\left(\frac{3-2x}{3-2y}\right)\right)MoSe_2$$

Here, the first to third terms on the right-hand side correspond to the substitutional embedding of Mo, formation of Bi_2 BLs and segregation of $MoSe_2$, respectively. Hence y corresponds to substitutional solubility $y \approx 0.001$.
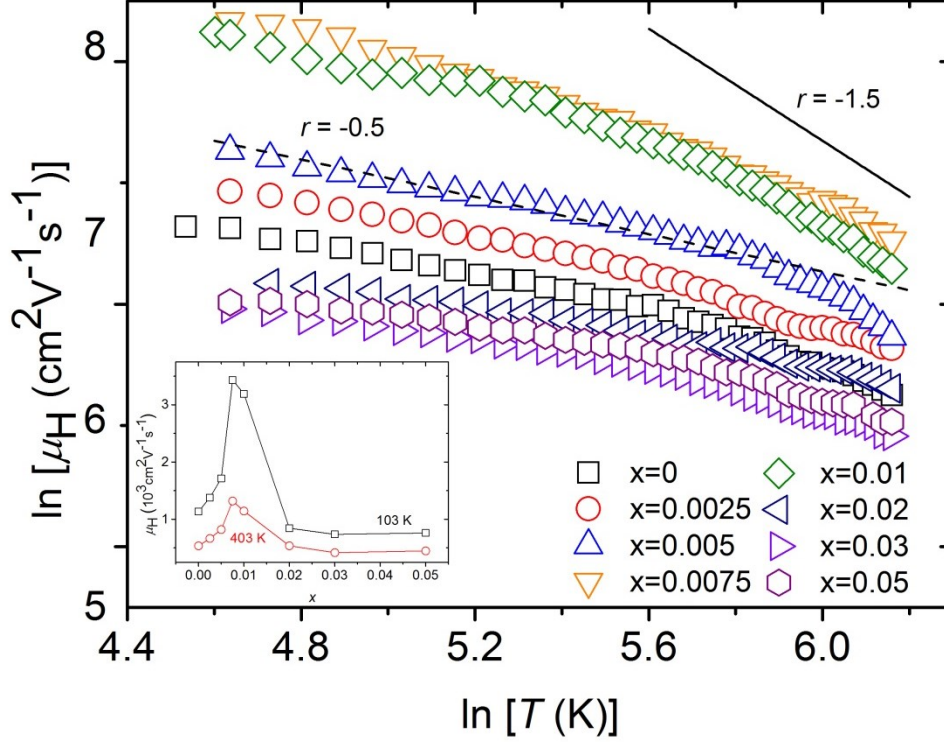
Fig. 16. Hall mobility μ as a function of temperature in log-scale for the Bi$_{2-x}$Mo$_x$Se$_3$ single crystals. The dashed and solid line represent the slopes r=-0.5 and r=-1.5 corresponding to the scattering by optical phonons and acoustic phonons. Note that the scattering by acoustic phonons dominates above T≈400 K, irrespective of the doping. Inset: Hall mobility as a function of the concentration x for the Bi$_{2-x}$Mo$_x$Se$_3$ single crystals for two different temperatures.

However, we encounter another rather troublesome point. According to high resolution XRD (HRXRD), the samples with highest mobility (x=0.005 – 0.01) show the most disordered structure. The undoped samples and the samples with $x \geq 0.02$ surprisingly show better structural ordering. The disorder clearly contradicts the healing process and high mobility of FCs. The present work shows that the disordered structure in Bi$_2$Se$_3$ is not essentially connected with low FC mobility. Rather, the opposite is true.
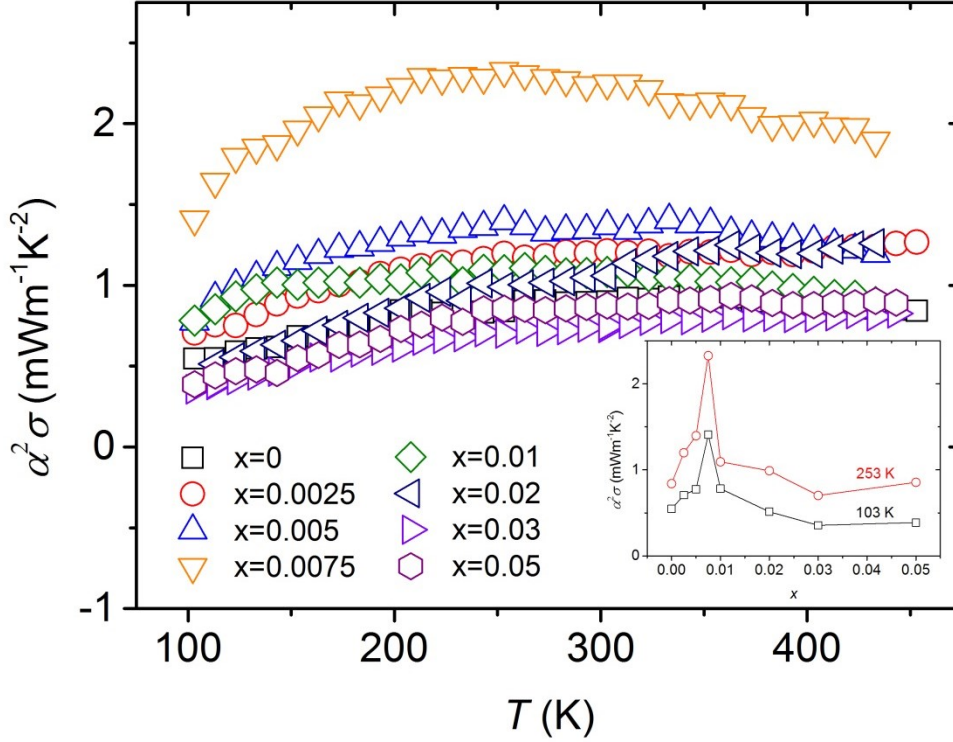
Fig. 17. Power factor PF as a function of temperature for the $Bi_{2-x}Mo_xSe_3$ single crystals. Inset: Power factor as a function of the concentration x for the $Bi_{2-x}Mo_xSe_3$ single crystals for two different temperatures.

The increase in PF may reflect either the increase in the mobility or a more favorable energy dependence by the mobility inducing, larger Seebeck coefficient α in terms of the Mott formula (eq. 5). Here, α depends on the logarithmic energy derivatives of the energy dependent FC concentration n (here, in fact, the density of states (DOS)) and of the energy dependent FC mobility μ around the Fermi level E_F:

$$\alpha = \frac{\pi^2 k_B^2 T}{3}\left\{\frac{1}{n}\frac{dn(E)}{dE} + \frac{1}{\mu}\frac{d\mu(E)}{dE}\right\}_{E=E_F} \tag{5}$$

The variation of the defect structure can enhance the second term in the parenthesis of eq. (1). A steep increase in the DOS, which increases the energy dependence of the FC concentration n and effective mass m_{ef} ($\mu = e\tau/m_{ef}$), is unlikely to occur due the parabolic band structure. In fact, these two contributions arising from n and m_{ef}, tend to cancel out. Thus, we are left with the energy-dependent relaxation time τ (eq. 2):

$$\frac{1}{\mu}\frac{d\mu(E)}{dE} \cong \frac{1}{\tau}\frac{d\tau(E)}{dE} \tag{6}$$

This term can account for a reasonably high Seebeck coefficient despite being produced by highly mobile electrons. This occurs on the background of a crossover from the scattering by point defects to the less energy demanding but more energy-dependent scattering by other defects (e.g., BLs, mosaicity).

Conclusion

We investigated the variation of the microstructure and transport properties of Bi_2Se_3 induced by Cr and Mo doping. Using the free melt crystallization (FMC), we prepared series of single crystalline samples $Bi_{2-x}Cr_xSe_3$ and $Bi_{2-x}Mo_xSe_3$ in composition range x = 0-0.04 and x = 0-0.05 (nominally), respectively, in a near equilibrium state at T = 823 K. Chromium and Molybdenum show an acceptor-like behavior, but their doping efficiency is rather low. The doping efficiency of Cr reaches approximately 10 %, Mo 30 % (i.e., ≈0.1 and 0.3 holes per atom). The true (substitutional) solubility of Cr in Bi_2Se_3 is x≈0.003 and Mo in Bi_2Se_3 x≈0.001.

In case of system $Bi_{2-x}Cr_xSe_3$, we assume the formation of nano-precipitates in the composition range (x = 0.003–0.02), as the X-ray diffraction analyses indicate the presence of additional phases ($BiCrSe_3$/$Bi_2Cr_4Se_9$) for $x \geq 0.02$. This conclusion is corroborated from the EDS/XRF/AFM analysis. The reciprocal space mapping reveals a modified mosaicity for the Cr-doped samples. We think the changes induced by the Cr doping lead to an extraordinary behavior of transport properties in Bi_2Se_3. The extraordinary behavior of the Seebeck coefficient and carrier mobility leads to an enhanced power factor in the doped crystals. In our view, this indicates the extraordinary energy filtering of free electrons. We suggest three possible mechanisms. First, the capture of electrons that is due to the mixed valence state Cr^{+2}/Cr^{+3}. Further, the formation of Cr compound-based nano-precipitates leads to the energy dependent scattering of electrons. Finally, the modified mosaicity can induce a favorable energy filtering of electrons. For TE applications, further modifications of the preparation route would be beneficial in terms of optimizing the nano-structuring. A modified kinetics of the preparation may lead, for example, to a higher concentration of smaller inclusions. The magnetization data corroborates the picture drawn from the transport data. Furthermore, the data indicates competing interactions of FM and AFM within the PM background of the diluted Cr solid solution in the Bi_2Se_3 matrix. Thus, it is worth exploring Cr-doped single crystals, especially in terms of the preparation route, as the kinetics and thermodynamics both play a role.

In case of system $Bi_{2-x}Mo_xSe_3$ additional phase ($MoSe_2$) appears for $x \geq 0.0075$. The amount of this phase is independent on the nominal concentration of the dopant. Due to the precipitation of $MoSe_2$ Mo doping shifts the composition of the matrix toward the Se-poor/Bi-rich state. The Se-poor composition induces the formation of Se vacancies, V_{Se}, Bi interstitials, Bi_i and antisites, Bi_{Se} (which are donors) in an undoped Bi_2Se_3. Hence, Bi_2Se_3 shows n-type conductivity. By contrast, the Se-poor composition lead to the formation of Bi_2 BLs in the Mo doped material as shown by AFM experiments. Thus, we conclude that Mo doping facilitates the formation of Bi_2 BLs and reduces the formation of the respective native defects. Since the formation of Bi_2 BLs strengthens the bonding between the QLs of Bi_2Se_3, it corroborates the depletion of native point defects induced originally by Mo doping in a "chicken and egg" scenario. The formation of BLs and depletion of the native point defects saturates at x≈0.01. According to the HRXRD and transport measurements, the further shift toward the Se-poor composition for x>0.01 recovers the original defect structure of Bi_2Se_3. Whether the formation of BLs may enhance the FC mobility of surface states remains an open question.

The present work shows that the disordered structure in Bi_2Se_3 is not necessarily accompanied by a low FC mobility. Rather, the opposite is true. This implies that the intrinsic FC mobility of the structure can be much higher than experimentally obtained value. The point defects (V_{Se}, , Bi_i and Bi_{Se}) represent barriers that are too high for the traveling electrons. However, it seems that the number of defects or their barriers can be lowered by doping. Thus, although we actually introduce additional defects by doping, we lowered the barriers and increased the FC mobility at the same time. We observed this effect for Cr-doped Bi_2Se_3 and in a more pronounced manner for the Mo-doped Bi_2Se_3. This implies that ionized impurity scattering may not be as favorable for the TE properties as believed. The energy barriers generated by e.g. V_{Se} seem to be detrimental for the mobility of the carriers and for PF. These results indicate that high mobility is more important than the scattering mechanism for reaching high PF. Furthermore, the TM induced mosaicity is expected to decrease the thermal conductivity, which is favorable for the TE efficiency (*ZT* values).

List of references

[1] Dyck, J. S., Drasar, C., Lostak, P., Uher, C., Phys. Rev. B 71 (2005) 115214.

[2] Kulbachinski, V. A., Tarasov, P. M., and Bruck, E., Physica B 368 (2005) 32–41.

[3] Kulbachinski, V. A., Tarasov, P. M., and Brück, E., JETP Letters, Vol. 81, No. 7, (2005) 342–345.

[4] Kulbachinski, V. A., Tarasov, P. M. and Brück, E., Journal of Experimental and Theoretical Physics, Vol. 101, No. 3, (2005) 528–534.

[5] Hor, Y. S., Roushan, P., Beidenkopf, H., Seo, J., Qu, D., Checkelsky, J. G., Wray, L. A., Hsieh, D., Xia, Y., Xu, S.-Y., Qian, D., Hasan, M. Z., Ong, N. P., Yazdani, A., and Cava, R. J., Phys. Rev. B 81 (2010) 195203.

[6] Pearton, S. J., Abernathy, C. R., Norton, D. P., Hebard, A. F., Park Y. D., Boatner, L. A., Budai, J. D., Mat. Sci. and Eng. R 40 (2003) 137.

[7] Zhang, H., Liu, C.-X., Qi, X.-L., Fang Y., and Zhang, S.-C., Nat. Phys. 5 (2009) 438-442.

[8] Chen, Y. L., Analytis, J. G., Chu, J.-H., Liu, Z. K., Mo, S.-K., Qi, X. L., Zhang, H. J., Lu, D. H., Dai, X., Fang, Z., Zhang, S. C., Fisher, I. R., Hussain, Z., Shen, Z.-X., Science 325 (2009) 178.

[9] Kuroda, K., Arita, M., Miyamoto, K., Ye, M., Jiang, J., Kimura, A., Krasowskii, E. E., Chulkov, E. V., Iwasawa, H., Okuda, T., Shimada, K., Ueda, Y., Namatame, H., and Taniguchi, M., Phys. Rev. Lett. 105 (2010) 076802.

[10] Xiao-Liang, Q, and Zhang, S.-Ch., Physics Today, 2010, 63(1).

[11] Moore, J., Nature Physics, 5 (2009), 378–380.

[12] Analytis, J. G., McDonald, R. D., Riggs, S. C., Chu, J.-H., Boebinger, G. S., and Fisher, I. R., Nature Physics, 6 (2010) 960-964.

[13] Matyas, M., Proceedings of the 12th International Conference on Physics of Semiconductors (ed. M. H. Pilkuhn), Stuttgart, Germany, 1974.

[14] Horak, J., Koudelka, L., Klikorka, J., and Sibka, L., Phys. Stat. Solidi (b), 111 (1982) 575.

[15] Weissenstein, J., Horak, J., Tichy, L., and Vasko, A., Cryst. Lattice Defects 8 (1980) 223.

[16] Kasparova, J., Drasar, C., Krejcova, A., Benes, L., Lost'ak, P., Chen, W., Zhou, Z. H., Uher, C., Journal of Applied Physics 97 (2005).

[17] Hor, Y. S., Richardella, A., Roushan, P., Xia, Y., Checkelsky, J. G., Yazdani, A., Hasan, M. Z., Ong, N. P., Cava, R. J., Phys. Rev. B, 79 (2009) 195208.

[18] Ren, Z., Taskin, A. A., Sasaki, S., Segawa, K., Ando, Y., Physical Review B 84 (2011).

[19] Chen, Z. L., Analytis, J. G., Chu, J.-H., et al. Science 325 (2009) 178.

[20] Choi, Y. H., Jo, N. H., Lee, K. J., Lee, H. W., Jo, Y. H., Kajino, J., Takabatake, T., Ko, K. T., Park, J. H., Jung, M. H., Applied Physics Letters 101 (2012) 152103.

[21] Kuroda, K., Arita, M., Miyamoto, K., et al., Phys Rev. Lett. 105 (2010) 076802.

[22] Androulakis, J., and Beciragic, E., Solid State Commun. 173 (2013) 5.

[23] Gao, Y. B., He, B., Parker, D., Androulakis, I., and Heremans, J. P., Phys. Rev. B. 90 (2014) 125204.

[24] Li, H., Song, Y. R., Yao, M.Y., Zhu, F. F., Liu, C.H., Gao, C.L., Jia, J. F., Qian, D., Yao, X., Shi, Y.J., Wu, D., Journal of Applied Physics 113 (2013).

[25] Yang, H., Liu, L. G., Zhang, M., Yang, X. S., Solid State Communications 241 (2016) 26-31.

[26] Singh, R., Shukla, K. K., Kumar, A., Okram, G. S., Singh, D., Ganeshan, V., Lakhani, A., Ghosh, A. K., Chatterjee, S., Journal of Physics-Condensed Matter 28 (2016).

[27] Kou, X. F., Jiang, W. J., Lang, M. R., Xiu, F. X., He, L., Wang, Y., Yu, X. X., Fedorov, A. V., Zhang, P., and Wang, K. L., J. Appl. Phys. 112 (2012) 063912.

[28] Liu, M., Zhang, J., Chang, C.-Z., Zhang, Z., Feng, X., Li, K., He, K., Wang, L.-L., Chen, X., Dai, X., Fang, Z., Xue, Q.-K., Ma, X., and Wang, Y., Phys. Rev Lett. 108 (2012) 036805.

[29] Haazen, P. P. J., Laloe, J.-B., Nummy, T. J., Swagten, H. J. M., Jarillo-Herrero, P., Heiman, D., and Moodera, J. S., Appl. Phys. Lett. 100 (2012) 082404.

[30] Choi, Y. H., Jo, N. H., Lee, K. J., Yoon, J. B., You, C. Y., and Jung, M. H., J. Appl. Phys. 109 (2011) 07E312.

[31] Kim, J., Jhi, S.-H., MacDonald, A. H., and Wu, R., Phys. Rev. B 96 (2017) 140410(R).

[32] Zhang, J.-M., Ming, W., Huang, Z., Liu, G.-B., Kou, X., Fan, Y., Wang, K. L., and Yao, Y., Phys. Rev. B 88 (2013) 235131.

[33] Shabunina, G. G., Kireeva, E. V., Aminov, T. G., Russ, J. Inorg. Chem. 41 (1996) 1496.

[34] Clarke, S. M., and Feedman, D. E., Inorg. Chem. 54 (2015) 2765.

[35] Bahk, J.-H., Bian, Z., Zebarjadi, M., Santhanam, P., Ram, R., Appl. Phys. Lett. 99 (2011) 072118.

[36] Faleev, S. V., and Leonard, F., Phys. Rev. B 77 (2008) 214304.

[37] Narducci D., Selezneva, E., Cerofoliny, G., Frabboni, S., Ottaviani, G., J. Solid State Chem. 193 (2012) 19.

[38] Deng, B., Liu, F., and Zhu, J., Phys. Rev. B 96 (2017) 174404.

[39] Seixas, L., Abdalla, L. B., Schmidt, T. M., Fazzio, A., Miwa, R.H., Journal of Applied Physics 113 (2013).

[40] Drouin, D., Couture, A. R., Joly, D., Tastet, X., Aimez, V., Gauvin, R., Scanning 29 (2007) 92.

List of Students' Published Works

Impact Factor Journals

[1] Alexander-Webber, J. A., Huang, J., Beilsten-Edmands, J., Čermák, P., Drašar, Č., Nicholas, R. J., and Coldea, A. I. Multi-band magnetotransport in exfoliated thin films of $Cu_xBi_2Se_3$. *J. Phys.: Condens. Matter* **30** (2018) 155302. DOI: 10.1088/1361-648X/aab193. ISSN: 0953-8984.

[2] Cermak, P., Ruleova, P., Holy, V., Prokleska, J., Kucek, V., Palka, K., Benes, L., Drasar, C. Thermoelectric and magnetic properties of Cr-doped single crystal Bi_2Se_3 − Search for energy filtering. *J. Solid State Chem.* **258** (2018) 768-775. DOI: 10.1016/j.jssc.2017.12.009. ISSN: 0022-4596.

[3] Cermak, P., Knotek, P., Ruleova, P., Holy, V., Palka, K., Kucek, V., Benes, L., Navratil, J., Drasar, C. High power factor and mobility of single crystals of Bi_2Se_3 induced by Mo doping. *J. Solid State Chem.* (*in press*). DOI: 10.1016/j.jssc.2019.07.045. ISSN: 0022-4596.

Conference Proceedings

[1] Čermák, P., Prokleška, J., Krejčová, A., Drašar, Č. Transport and magnetic properties of $Fe_xBi_2Te_3$ single crystals. In *Proceedings of the 4th International Conference on Chemical Technology*. Praha: Česká společnost průmyslové chemie, 2016. s. 274-278. ISBN 978-80-86238-94-4.

[2] Zich, J., Čermák, P., Janíček, P., Beneš, L., Drašar, Č. Studium termoelektrických vlastností monokrystalů sulfidu cínatého dopovaného thalliem. In *Sborník příspěvků: studentská vědecká odborná činnost 2017/2018*. Pardubice: Univerzita Pardubice, 2018. ISBN 978-80-7560-157-5.

Conference Talks

[1] Čermák, P. Tetradymitové polovodiče včera, dnes a zítra, *Veletrh věda, výzkum, inovace*, Brno (Czech Republic), 9.-11. 3. 2016.

[2] Čermák, P., Prokleška, J., Krejčová, A., Zvolská, M., and Drašar, Č. Transport and magnetic properties of $Fe_xBi_2Te_3$ single crystals, *26th Joint Seminar Development of Materials Science in Research and Education*, Pavlov (Czech Republic), 29. 8.-2. 9. 2016.

[3] Cermak, P., Drasar, C., Prokleska, J., Krejcova, A., Cernohorsky, T. Transport and magnetic properties of Bi_2Te_3 single crystals doped with overstoichiometric transition metal, *12th international conference Solid State Chemistry*, 2016. Prague (Czech Republic), 18. 9.-23. 9. 2016, ISBN 978-80-7080-969-3.

[4] Čermák, P. Výzkum termoelektrických materiálů na Univerzitě Pardubice, *Veletrh Věda Výzkum Inovace*, Brno (Czech Republic), 28. 2.-2. 3. 2017, ISBN 978-80-906697-2-7.

[5] Čermák, P., Plecháček, T., Beneš, L. and Drašar, Č. Doping Study of SnS, *27th Joint Seminar Development of Materials Science in Research and Education*, Kežmarské Žľaby (Slovak Republic), 4. 9.-8. 9. 2017, ISBN 978-80-89597-67-3.

[6] Cermak, P., Ruleova, P., Benes, L., Navratil, J., Drasar, C. Thermoelectric properties of Cr-doped single crystals Bi_2Se_3 – search for energy filtering, *15th European Conference on Thermoelectrics*, Padua (Italy), 25.-27. 9. 2017.

[7] Cermak, P., Plechacek, T., Hejtmanek, J., Levinsky, P., Svoboda, R., Zmrhalova, Z., Palka, K., Benes, L., Sraitrova, K., Drasar, C. Investigation of stability of Tl-doped SnS, *Development of Materials Science in Research and Education*, Pavlov (Czech Republic), 3.-7. 9. 2018. ISBN 978-80-905962-8-3.

[8] Cermak, P., Ruleova, P., Holy, V., Benes, L, Palka, K., Prokleska, J., Drasar, C. Extraordinary behavior of tetradymites doped with transition metals, *13th International Conference on Solid State Chemistry*, Pardubice (Czech Republic), 16.-21. 9. 2018. ISBN 978-80-7560-158-2.

Conference Posters

[1] Čermák, P., Drašar, Č., Prokleška, J., Krejčová, A., Transport and magnetic properties of $Fe_xBi_2Te_3$ single crystals, *4th International Conference on Chemical Technology*, Mikulov (Czech Republic), 25.-27. 4 2016, ISBN 978-80-86238-91-3

[2] Čermák, P., Plecháček, T., Beneš, L., and Drašar, Č. Study of Cation and Anion Doping of Pollycrystalline SnS on its Thermoelectric Properties – first hint, *5th International Conference on Chemical Technology*, Mikulov (Czech Republic), 10. 4.-12. 4. 2017, ISBN 978-80-86238-62-3.

[3] Holý, V., Kriegner, D., Wimmer, S., Bauer, G., Groiss, H., Springholz, G., Albu, M., Hofer, F., Caha, O., Drašar, Č., Čermák, P. High Resolution X-ray Diffraction from Epitaxial Layers and Bulk Crystals of Bi_mTe_n and Bi_mSe_n, *International Conference on Strongly Correlated Electron Systems*, Prague (Czech Republic), 17. 7.-21. 7. 2017.

[4] Čermák, P., Ruleová, P., Plecháček, T., Beneš, L., Frumarová, B., and Drašar, Č. Study of proper preparation route of thermoelectric binary chalcogenides, *6th International Conference on Chemical Technology*, Mikulov (Czech Republic), 16.-18. 4. 2018, ISBN 978-80-86238-83-8

[5] Cermak, P., Plechacek, T., Benes, L., Drasar, C. Investigation of stability of doped SnS, *37th International and 16th European Conference on Thermoelectrics*, Caen (France), 1.-5. 7. 2018